TiO₂/graphene-like photocatalysts for selective oxidation of 3-pyridine-methanol to vitamin B3 under UV/solar simulated radiation in aqueous solution at room conditions: The effect of morphology on catalyst performances

Michela Alfè [a], Danilo Spasiano [b,*], Valentina Gargiulo [a], Giuseppe Vitiello [b,c], Roberto Di Capua [d], Raffaele Marotta [b]

[a] Istituto di Ricerche sulla Combustione, Consiglio Nazionale delle Ricerche (IRC)-CNR, p.le V. Tecchio, 80, 80125 Napoli, Italy
[b] Dipartimento di Ingegneria Chimica, dei Materiali e della Produzione Industriale, Università di Napoli "Federico II", p.le V. Tecchio, 80, 80125 Napoli, Italy
[c] CSGI, Consorzio Interuniversitario per lo Sviluppo dei Sistemi a Grande Interfase, Italy
[d] Dipartimento di Fisica, Università di Napoli "Federico II", and SPIN-CNR UOS, via Cintia, 80126 Napoli, Italy

ARTICLE INFO

ABSTRACT

Graphene-like layers, synthesized through a two-step oxidation/reduction wet treatment of a high surface carbon black, have been used to prepare composites with TiO₂ nanoparticles by liquid phase deposition, followed by calcination at 200 °C. The photocatalytic activity of the TiO₂/graphene-like composites has been tested for the selective conversion of 3-pyridine methanol to 3-pyridine carboxyaldehyde and nicotinic acid (vitamin B3), under de-aerated and UV/solar simulated conditions, in the presence of cupric ions. Two different composite morphologies have been explored and a dependence of the photocatalytic activity has been assessed. An enhanced photocatalytic activity, with respect to the neat TiO₂, has been observed and attributed to the broader variety of stable free-radical species generated, at a given photo-catalyst morphology, within the delocalized π-electron systems.

© 2014 Elsevier B.V. All rights reserved.

1. Introduction

At the present time, there is a great interest to carry out the production of fine chemicals, under very mild conditions, using renewable energy sources, such as the solar radiation, and eco-friendly solvents, such as water [1,2]. To this aim the use of TiO₂-based photocatalysts appears to be advantageous as TiO₂ is easily available, stable to photocorrosion, cheap, and nontoxic substance [3–7].

When molecular oxygen accepts the TiO₂ photo-generated electrons in aqueous solution, it leads to the formation of HO radicals, which play highly negative role in these processes since they unselectively oxidize organic substrates:

$$TiO_2(e_{cb}^-) + O_2 \rightarrow O_2^{\bullet-} \ldots \rightarrow HO^{\bullet}$$
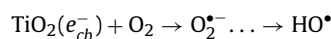
On the other hand, when metal ions, such as Cu(II) ions, are used in de-aerated conditions as electron acceptor instead of oxygen, the HO radical production is strongly limited and the process selectivity increases [8,9]. In particular, when Cu(II) ions accept the photo-generated conduction band electrons, they are reduced first to Cu(I) and then to Cu(0), which precipitate. Moreover, since the zero-valent copper could be simply re-oxidized to Cu(II), at the end of process, with an air flow blown into the solution in dark conditions, it is possible to consider also Cu(II) ions as co-catalysts [10].

However, even if the presence of oxygen is avoided through inert gas inlet during the photocatalytic process, the formation of HO radicals is not totally quenched, just resulting from the reaction of water molecules or surface adsorbed hydroxyl groups with positive holes [11]:

$$TiO_2(h_{vb}^+) + H_2O_{(ads)} \rightarrow TiO_2 + HO^{\circ} + H^+$$

$$TiO_2(h_{vb}^+) + H_2O_{(ads)}^- \rightarrow TiO_2 + HO^{\circ}$$
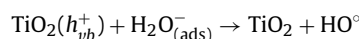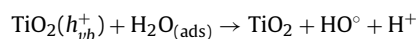
The produced hydroxyl radicals, attack the organic substrates and desired products, thus lowering the selectivity of the processes [8,10]. Moreover, one of the main problems associated with the use

* Corresponding author. Tel.:+39 0817682253; fax: +39 0815936936.
E-mail address: danilo.spasiano@unina.it (D. Spasiano).

of TiO$_2$ as a photocatalyst is the fast recombination reaction of the electron–hole pair:

$$TiO_2(h_{vb}^+) + TiO_2(e_{cb}^-) \rightarrow heat$$
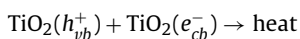
For this reason, many researchers are pointing their attention to the synthesis of different TiO$_2$-based catalysts containing inorganic and organic compounds, such as metal oxides, noble metals, graphene and copper sulphide [11–13], that decrease the electron–hole recombination. For example, it has been proven that the electron accepting and transport properties of graphene provide a convenient way to direct the flow of photo-generated charge carriers, which thus increases the lifetime of electron–hole pairs generated by TiO$_2$ upon light irradiation [14,15].

Direct TiO$_2$ growth on graphite oxide (GO) sheets followed by reduction of GO to graphene [16–20] has been proposed as possible strategy to produce composites that combine the electron accepting features of graphene and the TiO$_2$ photocatalytic activity. The use of the hydrophilic GO as intermediate step to obtain graphene is a convenient approach adopted to overcome the graphene aggregation driven by strong van der Waals forces when used in water and in polar organic solvents [14,21].

In the present investigation, direct TiO$_2$ growth on water-stable conductive graphene-like (GL) layers to produce TiO$_2$-based composite photocatalytic materials has been proposed. The GL layers, prepared in the present investigation, have a good stability in aqueous solutions and, undergo to self-assembling in flat blocks if dried on a flat surface thanks to the instauration of hydrophobic interactions between the graphenic layers. This behavior, typically observed in reduced graphite oxide [16], allowed to investigate different morphological arrangement of TiO$_2$/GL composites with the aim of studying the relationship between morphology and photocatalytic activity for a cleaner chemical production of vitamin B3.

The photocatalytic activities of the composites were tested by means of the selective oxidation of 3-pyridine methanol to 3-pyridine carboxyaldehyde and nicotinic acid, under de-aerated and UV/solar simulated conditions, in presence of cupric ions in aqueous solution at ambient temperature. Nicotinic acid (also known as niacin, vitamin PP or B3) is an important vitamin in B group and it is considered as one of the 80 essential human nutrients, largely used for the prevention and treatment of pellagra disease [23].

2. Experimental

2.1. Materials

Cupric ions were introduced in the system as cupric sulphate pentahydrate, (CuSO$_4$·5H$_2$O, ACS grade). 3-Pyridine methanol (3-PMA), 3-pyridine carboxyaldehyde (3-PCA), nicotinic acid (NA), copper sulphate, acetonitrile, ammonium acetate, hydrazine monohydrate (50 wt.%), thionin acetate (THA) salt (powder), ammonium hexafluorotitanate ((NH$_4$)$_2$TiF$_6$), boric acid, nitric acid (67 wt.%), and perchloric acid, were purchased from Sigma–Aldrich (ACS grade) and used as received. Carbon black (CB) type N110, produced with the furnace process, was obtained by Sid Richardson Carbon Co.

2.2. Preparation of neat TiO$_2$

Neat TiO$_2$ (in anatase form) was prepared according to the procedure reported by Jiang et al. [16]. 2.5 g of (NH$_4$)$_2$TiF$_6$ and 2.35 g of H$_3$BO$_3$ were dissolved in 125 mL of distilled water, sealed and stirred for 2 h at 60 °C. After cooling, the white solid was recovered through filtration (Anodisc, pore size 0.2 μm), washed with

distilled water, vacuum dried for 1 h and then calcined at 200 °C for 1 h.

2.3. GL layers synthesis

GL layers in water suspension were obtained through a two steps oxidation/reduction method [24] starting from a high surface carbon black (CB). Briefly, 500 mg of CB powder (15–20 nm primary particles diameter, specific BET area 139 m^2/g) was oxidized with 10 mL of nitric acid (67 wt.%) at 100 °C under stirring for 90 h. The oxidized carbon nanoparticles were recovered by centrifugation and washed until acid traces were successfully removed. Following the oxidation step, the nanoparticles (20 mg) were dispersed in 20 mL distilled water and treated with 450 μL of hydrazine hydrate (50%) at 100 °C under reflux for 24 h.

At the end of the reaction the excess of hydrazine was neutralized with nitric acid (4 M) and the resulting black solid recovered by centrifugation (3000 rpm, 30 min). The solid was washed with distilled water, recovered by centrifugation three times in order to remove traces of unreacted reagents and acid and named GL. The pH of the GL water suspension was 3.70. The dried GL resulted to be insoluble in water and in the most common organic solvents, both polar and apolar (water, ethanol, *N*-methyl pirrolidinone, dichloromethane, heptane, dimethylformamide (DMF) [23]). It was demonstrated by transmission electron microscopy (HRTEM) and atomic force microscopy (AFM) that the water-insoluble GL undergo to self-assembling in thin film on surfaces after drying [24]. The self-assembled film is made by pliant sheets that easily conform to any feature of that surface. The formation of flat film is associated with the decrease in the polar functionalities in GL layers as a consequence of the reduction step and subsequent intimate self-assembling interaction between the restored graphitic layers, as previously observed for the reduced graphite oxide [22].

Two strategies were adopted to produce the TiO$_2$-based composites, differing from the morphology of the GL layers: (1) freshly prepared GL layers in water suspension (GLW) were readily used; (2) GL layers (10 mg/mL) were allowed to dry at room temperature on a flat surface (glass surface). The resulted self-assembled product was scraped from the glass surface obtaining flat platelets of assembled GL layers (GL platelets, GLP).

2.4. Synthesis of TiO$_2$/GLW and TiO$_2$/GLP composites

Two composites were prepared by directly growing TiO$_2$ on GLW and GLP. TiO$_2$/GLW and TiO$_2$/GLP composites were prepared adapting the strategy reported by Jiang et al. for the preparation graphene oxide/TiO$_2$ composites [16]: 2.5 g of (NH$_4$)$_2$TiF$_6$ and 2.35 g of H$_3$BO$_3$ were dissolved in 125 mL of the GL (or GLP) aqueous suspension (75 mg/L) and stirred for 2 h at 60 °C. After cooling a grey solid was recovered by filtration (Anodisc, pore size 0.2 μm), washed with distilled water, vacuum dried for 1 h and then calcined at 200 °C for 1 h. The expected GL layers percentage is 5 wt.%

This approach aims to develop two composites with different morphology, as illustrated in Fig. 1. In the case of TiO$_2$/GLW, the GL and the TiO$_2$ precursors are well mixed in the reactive mixture allowing a good dispersion of GL into TiO$_2$. In the case of TiO$_2$/GLP, the GL layers are assembled in flat blocks offering a flat surface for the growing of TiO$_2$ crystal.

2.5. Characterization procedure

The thermal stability of the prepared samples was evaluated by using thermogravimetric analysis (TGA) performed on a Perkin-Elmer Pyris 1 Thermogravimetric Analyzer. The materials were heated in an oxidative environment (air, 30 mL min^{-1}) from 50 °C up to 750 °C at a rate of 10 °C min^{-1}.
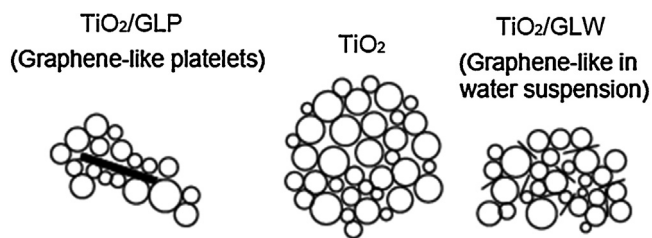
Fig. 1. Representation of the hypothesized morphologies of TiO₂/GLW and TiO₂/GLP composites.

The Brunauer–Emmet–Teller (BET) specific surface areas of the samples were measured by N_2 adsorption at 77 K using a Quantachrome Autosorb 1-C. The samples were outgassed under vacuum at 110 °C before the analysis. Adsorption/desorption data were processed in accordance with the Barrett–Joyner–Halenda (BJH) model.

X-ray diffraction (XRD) analysis was carried out using a Philips PW1710 diffractometer operating between 5 and 80 2θ with a Cu Kα radiation. A diffraction experiment was run on standard glass slide for the background correction.

The determination of surface acidic functionalities was performed according to the fluorimetric test reported by Visentin et al. [25]. The carbonaceous material (0.01 mg) was treated with 1.5 mL of a solution of THA in ethanol (4.3×10^{-6} M) for 30 min under continuous stirring at room temperature. The suspension was filtered on a 20 nm filter unit (Anotop 25, Whatman) and the fluorescence emission was measured with a Perkin-Elmer LS 50 B spectrofluorimeter (scan speed 100 nm/min, emission recorded in the range between 570 and 700 nm upon excitation at 594 nm).

Scanning Electron Microscopy (SEM) was performed on a FEI Inspect™ S50 Scanning Electron Microscope. Analysis was realized on a powder sample previously dried and sputter coated with a thin layer of gold to avoid charging.

Electron Paramagnetic Resonance (EPR) Spectroscopy was carried out by means of X-band (9 GHz) Bruker Elexys E-500 spectrometer (Bruker, Rheinstetten, Germany), equipped with a super-high sensitivity probe head. Solid samples were transferred to flame-sealed glass capillaries which, in turn, were coaxially inserted in a standard 4 mm quartz sample tube. Measurements were performed at room temperature. The instrumental settings were as follows: sweep width, 100 G; resolution, 1024 points; modulation frequency, 100 kHz; modulation amplitude, 1.0 G. The amplitude of the field modulation was preventively checked to be low enough to avoid detectable signal overmodulation. Preliminarily, EPR spectra were measured with a microwave power of ~0.6 mW to avoid microwave saturation of resonance absorption curve. Several scans, typically 16, were accumulated to improve the signal-to-noise ratio. Successively, for power saturation experiments, the microwave power was gradually incremented from 0.02 to 160 mW. The g-factor value was evaluated by means an internal standard (TEMPOL ethanol solution) [26] which was inserted in the quartz sample tube co-axially with the capillary containing the GL in water suspension or composite samples. Free radical concentration in the sample was estimated by using a TEMPOL ethanol solution as reference, whose concentration was determined by UV spectroscopy [27]. The area under the EPR absorption curves was estimated by double integration of their first derivatives.

Non-contact Atomic Force Microscopy (NC-AFM) was employed to characterize the GL building-blocks. NC-AFM morphological characterization was carried out by means of an XE100 Park instrument operating in non-contact mode (amplitude modulation, silicon nitride cantilever from Nanosensor) at room temperature and in ambient conditions. Samples for NC-AFM imaging were prepared by drop-casting a very low-concentrated GL water-suspension (0.1 µg/mL) onto freshly cleaved mica substrates (grade V-1, Electron Microscopy Sciences), which were then allowed to dry in air.

2.6. Photocatalytic reactor equipment and analytical procedure

The photocatalytic runs were performed, in duplicate, in an annular batch glass reactor (V 0.280 L, external diameter 6.5 cm, height 40 cm and optical path 1.1 cm), equipped with a mercury vapor high pressure lamp (nominal power 125 W, Helios Italquartz) mainly emitting at 305, 313 and 366 nm (manufacturer data). The photon flows of the lamp at 305, 313 and 366 nm, determined through actinometric analysis, were 4.85×10^{-5}, 8.34×10^{-5} and 2.71×10^{-4} E/min, respectively. The reactor was thermostated at 25 °C by using a thermostat bath (Julabo ED-13) and stirred magnetically. The apparatus device has been reported elsewhere [28].

Before turning on the lamp, the aqueous solution, containing the organic substrate ([3-PMA]o = 1.5 mM), cupric salts ([CuSO₄]o = 1.5 mM) and a proper load of catalyst (TiO₂ = 570 µg/mL, TiO₂ composites = 600 µg/mL) was purged with a nitrogen stream for 30 min at dark (flow rate = 0.3 L/min). The different catalyst load has been chosen to account the effective TiO₂ content in TiO₂ composites. (30 µg/mL being the GL amount, 5% of 600 µg/mL).

The photocatalytic runs were carried out under inert atmosphere to prevent the inlet of oxygen and the external walls of the reactor were covered with an aluminum foil to prevent the dispersion of the light emitted by the lamp.

The pH was adjusted at the desired value (pH 3.0) with perchloric acid (pH-meter Orion 420A+ by Thermo).

The samples, taken from the reactor at different reaction times, were filtered on regenerated cellulose filters (0.45 µm, Teknokroma) and analyzed by high performance liquid chromatography (HPLC) using an Agilent 1100 instrument equipped with a diode array UV–vis lamp (265 nm) and a Synergy 4u MAX-RP 80A column (flow rate 1.0 mL/min, 30 °C). The adopted gradient elution was 95% of buffer solution (ammonium acetate 20 mM) and 5% of acetonitrile for 5 min, rise to 75% of buffer solution and 25% of acetonitrile in 10 min. The concentration of dissolved copper, was measured by means of a colorimetric method with an analytical kit (based on oxalic acid bis-cyclohexylidenehydrazide, cuprizone®) purchased from Macherey-Nagel. A UV–vis spectrometer (Unicam) was used to measure the dissolved copper at a wavelength of 585 nm. A detection limit of 0.1 mg/L was found during this investigation.

3. Results and discussion

3.1. GLW and GLP characterization

GL layers in water suspension (GLW) consist of small flat nanoparticles decorated at the edge with oxygen-containing groups (mainly carboxylic/carbonylic and hydrazones) with graphenic basal plane untouched [23]. The carboxylic functional groups, residual from the reduction treatment of strongly oxidized CB, have been quantified by a sensitive and fast fluorimetric method [25]. The amount of acid groups was estimated to be 9.4×10^{-8} mol$_{COOH}$/mg. The presence of residual carboxylic functional groups allows a good stability and dispersion of GL sample in aqueous solution.

When GL layers in water suspension were allowed to dry on a flat surface, they underwent to self-assembling forming a flat film whose height depends upon the concentration of the starting solution. NC-AFM morphological characterization of ultrathin films (<20 nm) obtained from GL drying has been reported elsewhere [24], providing a surface characterization and roughness
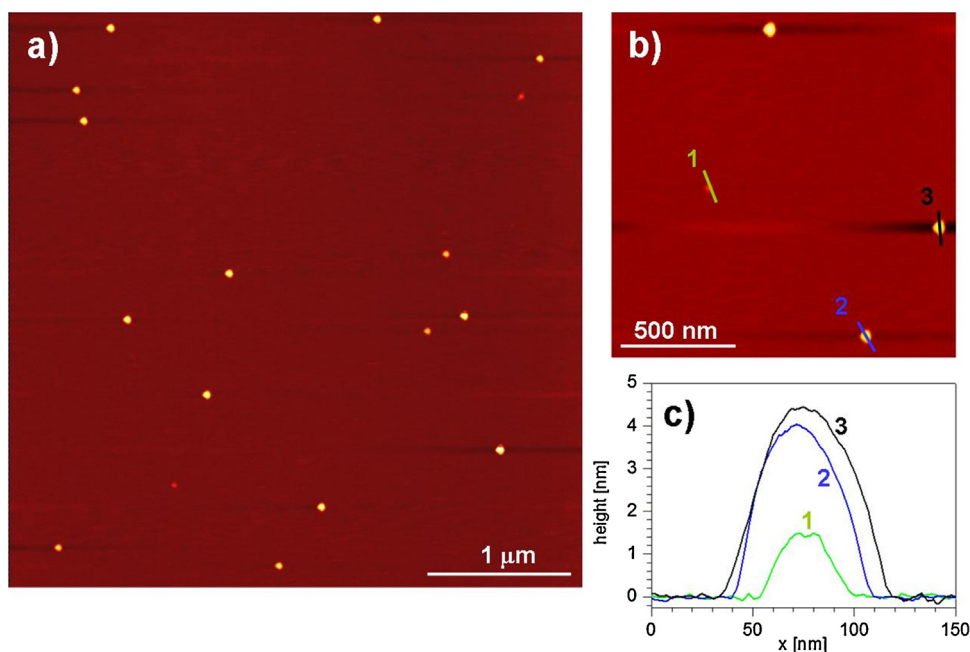
Fig. 2. AFM characterization: (a) NC-AFM topographic image, 4 μm × 4 μm, showing the presence of GL nanoparticles on a mica substrate; (b) NC-AFM topographic image, 1.5 μm × 1.5 μm, zoomed on some representative nanoparticles, reporting the analyzed profiles positions; (c) height profiles on GL nanoparticles, taken along the lines highlighted in panel (b).

estimation. Here, the observation of the GL layers, which are at the basis of the GLP formation, is reported. The freshly cleaved mica used as substrate guarantees an atomically flat underlying surface, which is needed for the correct observation and size measurements of particles on a nanometer scale. In addition, a very low-concentrated water-suspension (0.1 μg/mL) was used for drop-casting onto mica substrate. Such a low value was chosen in order to prevent the formation of aggregates on the substrate, allowing instead the achievement of rather individual GL layers. The concentration of water suspension, however, was high enough to allow the presence of a certain number of nanoparticles per unit area of the substrate, so that to be easily detectable in the scanning area of the microscope.

Fig. 2 shows the presence of nanoparticles deposited on the mica flat surface. A detailed characterization of such particles reveals a size distribution, which can be ascribed to different aggregation amounts of elementary constituents. Selected height profiles crossing the particles demonstrate first of all, the flatness of the substrate (the measured roughness, of the order of 1 Angstrom, is undistinguishable from the noise level of the instrument, and anyway well below the height of the particles under study), and its suitability for a reliable characterization of the nanoparticles. From such profiles we observed vertical sizes ranging from about 1 nm or less to few nanometers; the larger lateral dimensions, a few tens of nanometers (about 50 nm), confirms that at the chosen concentration of water suspension some aggregations are still occurring.

When a concentrated GL water suspension (10 mg/mL) was allowed to dry on a flat surface, a carbonaceous film is formed. The production of flat blocks about 1–2 μm thick (Fig. 3) was achieved by scraping the carbonaceous film. These flat blocks, here named GL platelets (GLP), offer a larger surface for TiO_2 growing.

During the hydrolysis of $(NH_4)_2TiF_6$, used as TiO_2 precursor, titanium hydroxide complex ions were gradually produced and further form TiO_2 nanoparticles [16]. The residual oxygen-containing groups on the GLW and GLP surface, not present on the raw CB surface and introduced after the oxidation-reduction treatment, can interact with titanium hydroxide complex ions and the growing TiO_2 nanoparticles through hydrogen bonds. These

interactions favor the nucleation of TiO_2 nanoparticles on GLW and GLP surface.

3.2. TiO_2 and composites characterization

3.2.1. XRD analysis

The X-ray diffraction patterns of the prepared samples are reported in the 20–80 2θ range (Fig. 4). The diffraction pattern of neat TiO_2 confirms that the sample is present in the anatase form (JCPDS 21-1272). The XRD path of both composites showed that the production of TiO_2 in the anatase form is not influenced by the addition of GL layers. Nevertheless, low intensity signals attributed to rutile contamination (as 2θ = 27.5, (1 1 0) diffraction peak) in TiO_2-GLW XRD pattern were also detected. There were no observable peaks of the GL layers in both the composite samples, possibly due both to the relatively low content of carbonaceous material in the composites and to their low intensity, compared to the prevailing TiO_2 pattern. The peak at 2θ = 25.2 (1 0 1 diffraction peak) for the TiO_2/GLP sample is higher with respect to the neat TiO_2, whereas the TiO_2/GLW exhibits a lower intensity peak. This result indicates a higher crystallinity of TiO_2/GLP. It can be speculated that the presence of well dispersed GL layers into the TiO_2/GLW composite interferes with the TiO_2 crystallization process whereas GLP offers a flat surface advantageous for TiO_2 growing and crystallization.

3.2.2. SEM analysis

The morphology of the TiO_2/GLW and TiO_2/GLP composites was observed with SEM (Fig. 5). Neat TiO_2 is also reported for comparison. The dimensions of the composites range in the micrometer scale: the granulometric analysis performed on the samples shows that the particle size distribution is lower than 20 μm which allows an easy separation of the composites by filtration. Neat TiO_2 anatase exhibits rather spherical primary particles which aggregate forming larger particles. The morphology of the composites is similar to that exhibited by neat TiO_2 and no significant differences are observable.
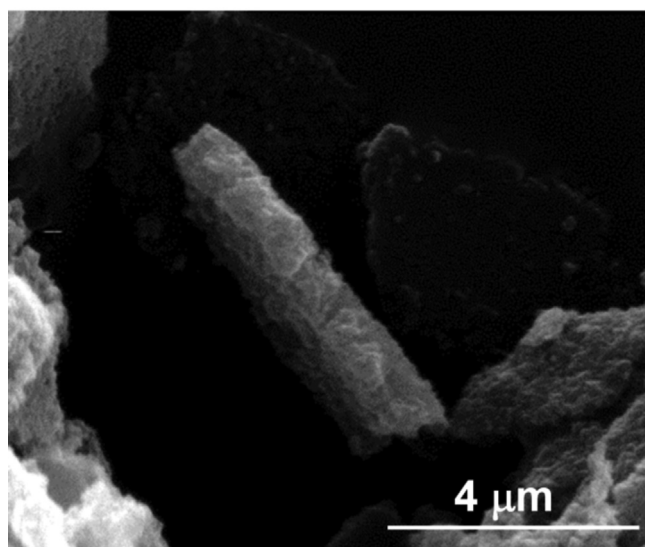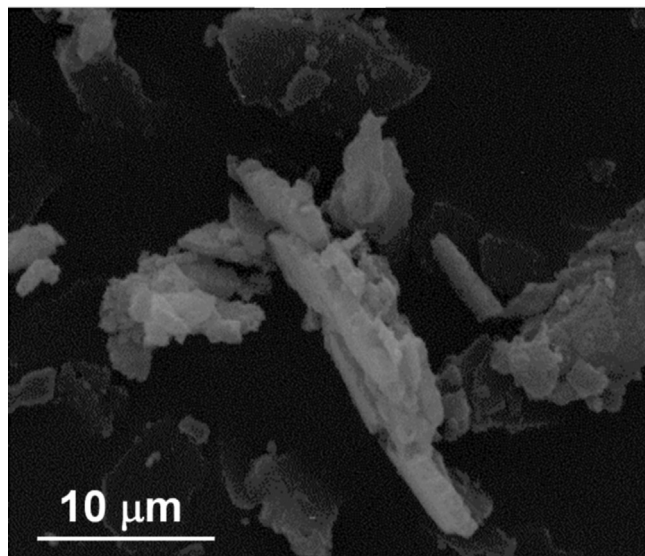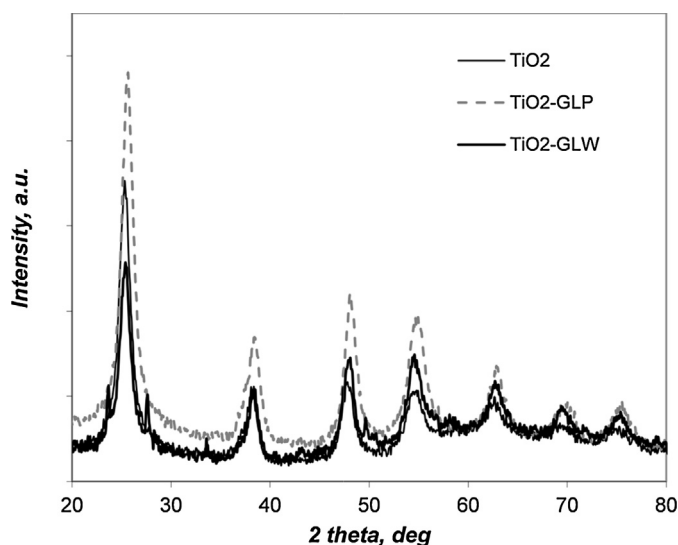
Fig. 3. SEM images of GLP.

Fig. 4. XRD patterns of TiO$_2$/GLW and TiO$_2$/GLP composites and neat TiO$_2$.

Table 1
EPR spectral parameters for TiO$_2$/GLW, TiO$_2$/GLP and neat GLP powders.

	GLP	TiO$_2$/GLP	TiO$_2$/GLW
g-factor	2.0040 ± 0.0004	2.0035 ± 0.0004	2.0037 ± 0.0004
ΔB (G)	3.3 ± 0.2	2.9 ± 0.2	1.6 ± 0.2
Spin × g^{-1}	1.4 × 10^{14}	8.5 × 10^{13}	4.9 × 10^{14}

3.2.3. BET analysis

N$_2$ adsorption/desorption measurements with BET method were carried out to determine the surface area of the samples. TiO$_2$/GLP composite had a surface area of 106.9 m^2/g, higher than the values measured for the neat TiO$_2$ and GLP that are 85 and 76 m^2/g, respectively. The increase of the surface area is not deducible by a weighted average of the two neat components (GLP and TiO$_2$) indicating the occurrence of non-additive effects due to the incorporation of the GLP component. A higher surface area was exhibited by TiO$_2$/GLW (138 m^2/g) and was interpreted as a consequence of a more defective and irregular surface due to the interference of GL in the TiO$_2$ crystallization process (Figs. 2 and 3).

3.2.4. TGA analysis

Fig. 6 shows the TGA curves in oxidative environment (air) for the TiO$_2$/GLW and TiO$_2$/GLP composites. Neat GLP was also reported for comparison. The GLP sample exhibits two weight losses, the first one between 150 and 500 °C (~40% of total weight loss) due to the progressive decomposition of residual oxygen-containing groups (carbonylic/carboxylic), and the second one at 550 °C due to the bulk oxidation of GLP. Interestingly, the curve for the TiO$_2$/GLW composite does not exhibit the clear steps of mass loss at about 550 °C as TiO$_2$/GLP suggesting that the GL layers are well-mixed within the composite and stabilized by the deposited TiO$_2$ through the interaction between oxygen-containing groups on the GL and TiO$_2$ particles. According to the TGA curves, in both composites the weight content of GL layers was roughly evaluated to be 3–4 wt.%, slightly lower than the expected percentage (5 wt.%).

3.2.5. EPR analysis

EPR measurements on TiO$_2$/GLW and TiO$_2$/GLP composites were performed by following an experimental procedure recently used in the characterization of melanins [29–31]. Analysis of this EPR signal provides significant information on the nature of the para-magnetic centers and on the supramolecular properties of solid materials. In this study, we undertook an EPR characterization of powdered samples synthesized as previously described. Neat TiO$_2$ and GLP were used as references. All EPR spectra are reported in Fig. 7, whereas the spectral parameters calculated from them are summarized in Table 1.

By observing Fig. 7, no signal was detected for neat TiO$_2$ (spectrum A), indicating no oxygen vacancy or Ti^{3+} in this powder which is consistent with a previous report that indicates no EPR signal for pure TiO$_2$ [32]. In Fig. 7, the spectra B, C and D represent the spectra of neat GLP, TiO$_2$/GLP and TiO$_2$/GLW respectively. They present a similar lineshape: a single, roughly symmetric signal at a *g* value of ~2.0035–2.0040, (Table 1), typical of carbon-centered radicals. It is in agreement with the literature [33,34] and corresponds to the samples with a high content of carbon which have more para-magnetic centers. In particular, Nakamura et al. attributed the EPR signal at this position to an oxygen vacancy [35], whereas no other detectable signal, such as Ti^{3+} or O^{2-}, appears in our tests. Since the signals of the two composites (Fig. 7, spectra C and D) present the same lineshape observed for the GLP (Fig. 7, spectrum B), the emergence of the oxygen vacancy in the hybrid TiO$_2$ samples is directly dependent on the presence of GL layers in the composite synthesis, in according to the literature findings [34].
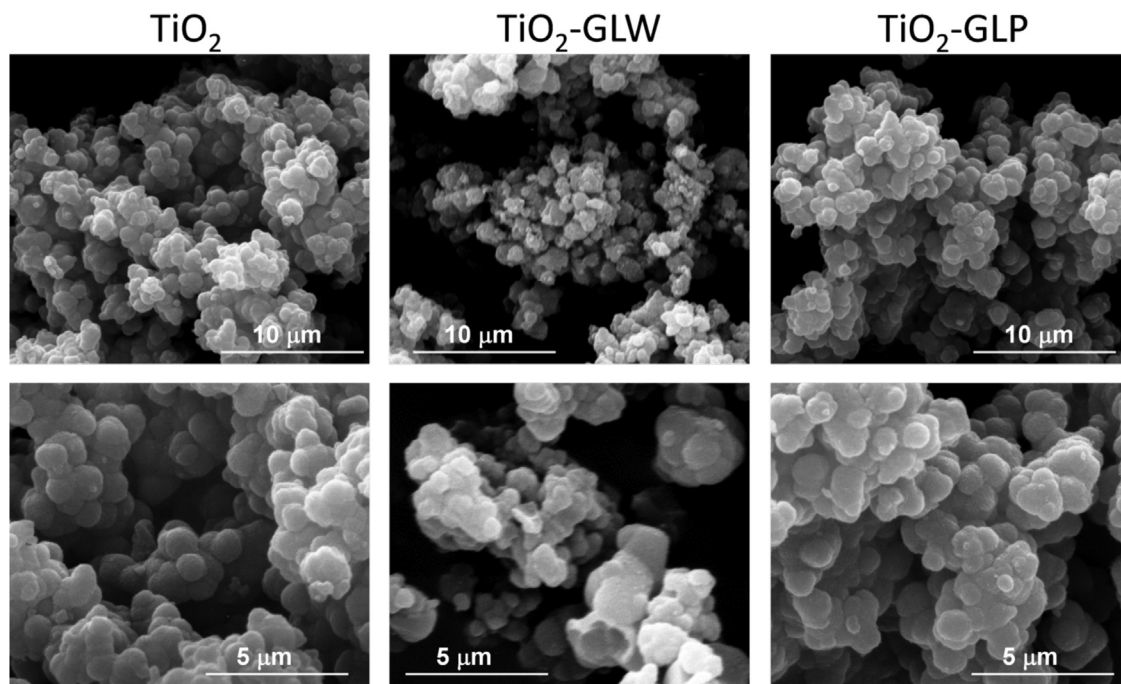
Fig. 5. SEM images for TiO$_2$/GLW and TiO$_2$/GLP composites and neat TiO$_2$.

However, a deeper analysis of the spectra of composites shows that the TiO$_2$/GLP spectrum is evidently broader than the TiO$_2$/GLW one. The difference in lineshapes was corroborated by the quantitative determination of the signal amplitude (ΔB). The ΔB value determined from the spectrum of TiO$_2$/GLP is significantly lower than those derived from the spectrum of TiO$_2$/GLP which is comparable to GLP spectrum (Table 1). To ascertain physical reasons for this experimental evidence, the EPR spectra of the same samples were acquired setting a higher microwave power. An inspection of the normalized power saturation profiles, reported in Fig. 8, shows that, as the microwave power is increased, the spin density increases. Also, the power saturation curve of TiO$_2$/GLP (and similarly of pure GLP) does not go to a plateau, in contrast to that observed in the case of TiO$_2$/GLW. The comparatively low ΔB value and the power saturation profile of TiO$_2$/GLW would suggest a relatively homogeneous free-radical species distribution that is spatially confined within restricted region of the catalyst supramolecular structure, in contrast to the broader variety of free-radical species that could be generated within the delocalized
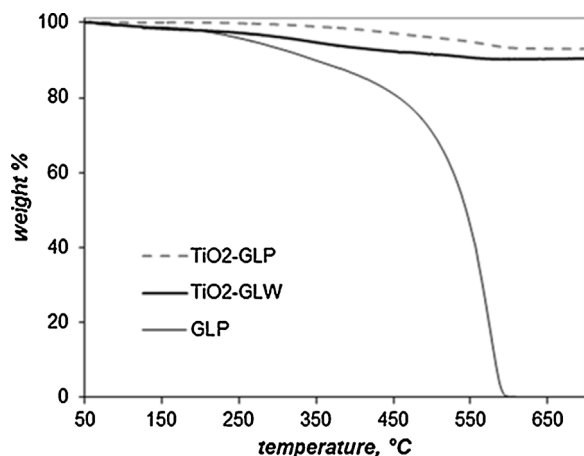
π-electron systems of the TiO$_2$/GLP. The reduced "mobility" of free radicals, generated under irradiation, is interpreted as an interruption of the electron "mobility" within the graphene-like, dispersed over the TiO$_2$ matrix but not grouped in platelet as in the case of TiO$_2$/GLP [34]. This property, added to the presence of oxygen vacancies, probably contributes to improve the photocatalytic activity of the catalyst, as also suggested in literature [33]. Different studies have proposed that the defects in the material structure have a significant effect on the electronic states of the entire flake of graphene. These defects can increase the electrons mobility which is directly correlated to the material conductivity [36]. Finally, a
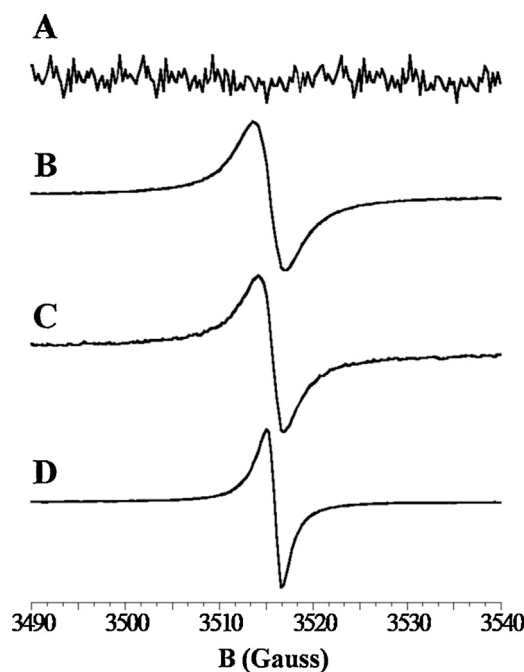

Fig. 6. TGA curves of TiO$_2$/GLW and TiO$_2$/GLP composites and GLP.

Fig. 7. EPR spectra of neat TiO$_2$ (**A**), neat GLP (**B**), TiO$_2$/GLP (**C**) and TiO$_2$/GLW (**D**) composites.
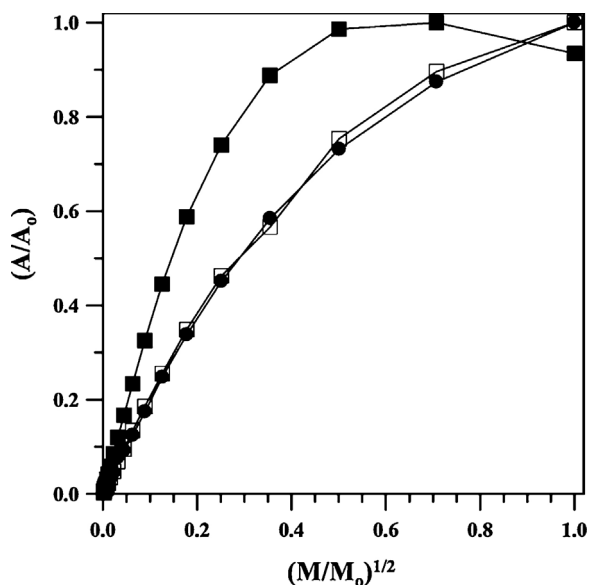
Fig. 8. Influence of microwave power on amplitudes of free radicals of GLP ($\square$), TiO$_2$/GLP ($\bullet$) and TiO$_2$/GLW ($\blacksquare$) composites.

quantitative analysis of the spectra intensities shows that all samples present a similar high spin density (Table 1).

3.3. Composites photocatalytic activity

Composites were tested to check their photocatalytic activity for the partial oxidation of 3-pyridine methanol (3-PMA) to 3-pyridine carboxyaldehyde (3-PCA) and nicotinic acid (NA) under illuminated and deaerated conditions in the presence of cupric ions, used as photoelectron scavengers.

The normalized concentration profiles for 3-PMA and dissolved copper, and the reaction yields for 3-PCA and NA, under different experimental adopted conditions, are reported in Figs. 9a–d respectively.

The homogenous system, in the only presence of CuSO$_4$ (empty triangles), shows a low reactivity probably ascribed to a photocatalytic activity of the Cu(II)/3-PMA complexes. The addition of the sole GL or GLP to the aqueous solution, containing cupric ions and 3-PMA, does not improve the system reactivity with respect the previous one (empty squares and diamonds).

A marked increase of 3-PMA and Cu(II) consumption, and 3-PCA and NA production rates was achieved in presence of cupric ions with neat TiO$_2$ catalyst at a load of 570 µg/mL (full squares).
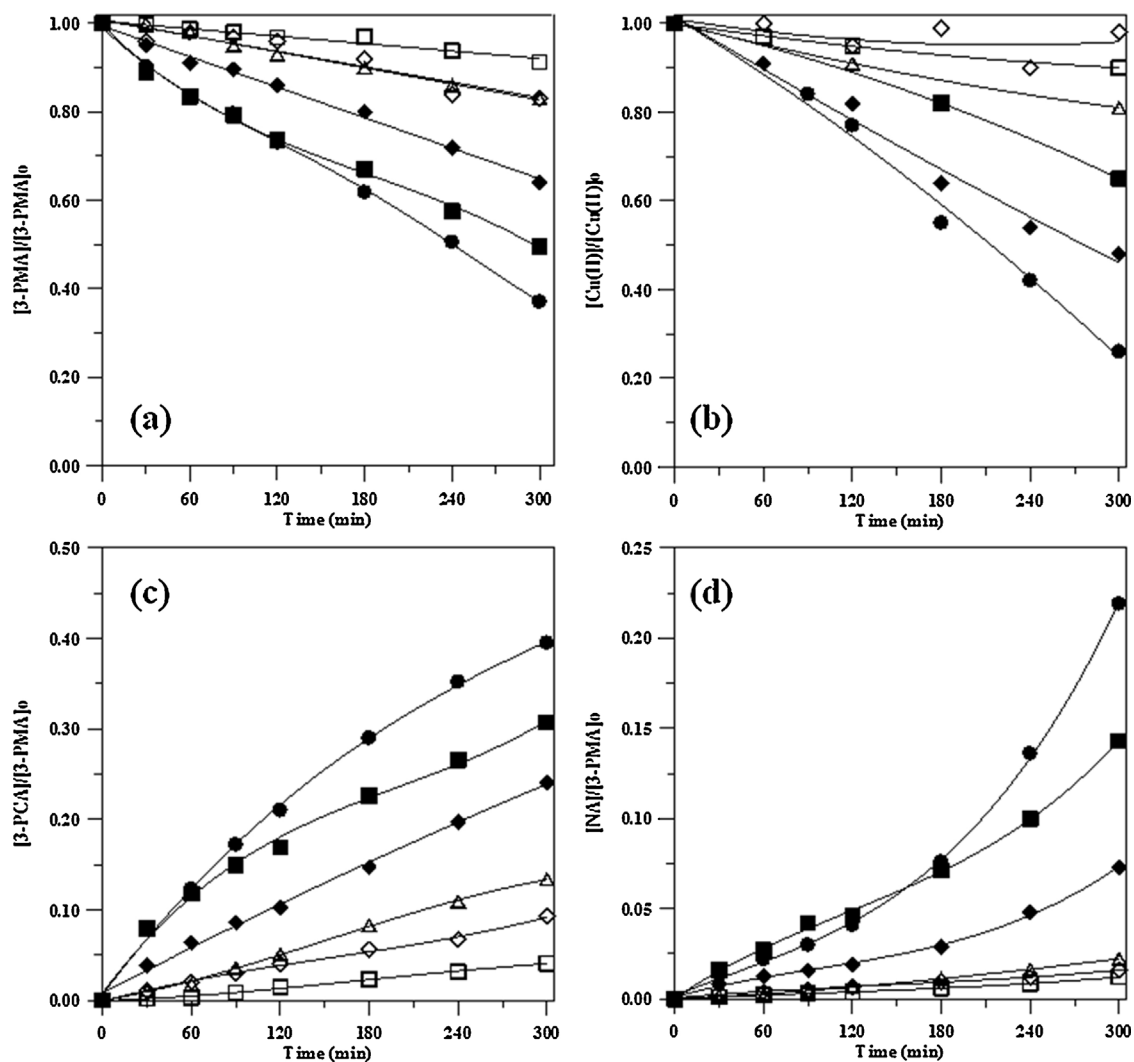

Fig. 9. Selective photo-oxidation of 3-PMA at different experimental conditions under deaerated conditions: (a) 3-PMA consumption; (b) Cu(II) photoreduction; (c) 3-PCA yield; (d) NA yield. [3-PMA]$_o$ = 1.5 mM, [CuSO$_4$]$_o$ = 1.5 mM; pH 3.0; T = 25 °C. In presence of TiO$_2$/GLP, load 600 ppm ($\bullet$); neat TiO$_2$, load 570 ppm ($\blacksquare$); TiO$_2$/GLW, load 600 ppm ($\blacklozenge$); GLP only, load 50 ppm ($\square$); GLW only, load 50 ppm ($\diamond$); CuSO$_4$ only ($\triangle$).

Table 2
Photocatalytic selective oxidation of 3-PMA in presence of $CuSO_4$ and different solid samples (neat TiO_2, neat GL, neat GLP and composite catalysts) for a reaction time of 5 h. Conversion (X), yield (Y), selectivity (S).

| Run	Catalyst	$X_{(3-PMA)}$ (%)	$Y_{(3-PCA)}$ (%)	$S_{(3-PCA)}$ (%)	$Y_{(NA)}$ (%)	$S_{(NA)}$ (%)	Carbon mass balance (%)
1	Only $CuSO_4$	17.3	13.4	77.4	2.23	12.8	98.0
2	$CuSO_4$ and neat GL	12.4	9.14	73.7	1.63	13.1	98.2
3	$CuSO_4$ and neat GLP	8.44	4.08	48.3	1.21	14.3	96.3
4	$CuSO_4$ and neat TiO_2	50.2	30.7	61.1	14.3	28.5	94.6
5	$CuSO_4$ andTiO_2/GLW	35.8	24.1	67.3	7.28	20.3	94.4
6	$CuSO_4$ and TiO_2/GLP	63.3	39.5	62.4	21.9	34.6	97.9

$[3-PMA]_o = 1.5$ mM; $[CuSO_4]_o = 1.5$ mM; pH 3.0; $T = 25\,°C$.

The composites, present in the reacting system at a load of 600 μg/mL to account the effective TiO_2 content (95 wt.%), show very different catalytic activities depending on the morphology of GL layers (GLW or GLP) added to the system.

When TiO_2/GLW was used as catalyst (full diamonds), the reactivity is even lower than that in which neat TiO_2 is present. On the other hand, the photocatalytic oxidation rates of 3-PMA, the cupric ions reduction rates and the yields to 3-PCA and NA were rather increased in the presence of TiO_2/GLP (full particles) at the same adopted experimental conditions.

The collected results indicated that, under the adopted experimental conditions, the production of NA for photocatalytic oxidation of 3-PMA, proceeds through the following steps:
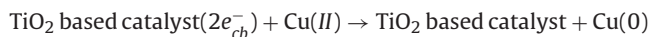
1) photogeneration of holes and electrons

$$TiO_2 \text{ based catalyst} \xrightarrow{h\nu} TiO_2 \text{ based catalyst}(e_{cb}^-, \, h_{vb}^+)$$
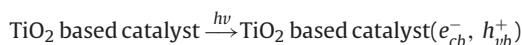
2) formation of 3-PCA, as primary chemical intermediate, by reaction of holes with 3-PMA

$$TiO_2 \text{ based catalyst}(2h_{vb}^+) + 3\text{-PMA} \rightarrow TiO_2 \text{ based catalyst}$$
$$+ 3\text{-PCA}$$
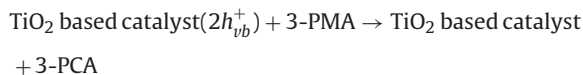
3) conversion of 3-PCA to NA

$$TiO_2 \text{ based catalyst}(2h_{vb}^+) + 3\text{-PCA} \rightarrow TiO_2 \text{ based catalyst} + NA$$

4) photoreduction of cupric ions to copper zero-valent

$$TiO_2 \text{ based catalyst}(2e_{cb}^-) + Cu(II) \rightarrow TiO_2 \text{ based catalyst} + Cu(0)$$

A summary of the conversion degrees for 3-PMA and selectivities and yields to 3-PCA and NA, along with the carbon mass balance, after 5 h of reaction time, is reported in Table 2. First, the presence of GL layers in water suspension or GLP only (runs 2 and 3) does not provide any improvement compared to the homogeneous system (run 1). On the contrary, the addition of neat TiO_2 only (run 4) involves an increase of the conversion degree up to 50% and yields to 3-PCA and NA up to 31% and 14%. Whereas the overall selectivity (87.3%) and the carbon mass balance (94.4%) are almost the same, the use of TiO_2/GLW as photo-catalyst (run 5) involves a reduction of the conversion degree (35.8%) and yield (24% and 7.3) if compared to the use of neat TiO_2.

On the contrary, the use of TiO_2/GLP as photo-catalyst (run 6) results in improved of the 3-PMA conversion degree (63.3%) and yield (39.5% for 3-PCA and 22% for NA). Moreover, higher values for the global selectivity (97%) and the mass carbon balance (98%) are achieved. The TiO_2/GLP catalyst, compared to neat TiO_2 and TiO_2/GLW catalyst, promotes the selective oxidation of 3-PMA to 3-PCA and of 3-PCA to NA.

It has been reported that the photocatalytic activity of TiO_2 is strongly affected by several parameters such as the phase structure, crystal size, specific surface area and crystallinity [37,38]. In order to achieve better photocatalytic performances, a good crystallinity is often required to reduce the formation of electron traps, which might affect the photocatalytic efficiency [39]. Moreover, a catalyst with a large specific surface area may be also desirable since the contact between the active sites and the reacting substances is enhanced.

The lower photocatalytic activity of TiO_2/GLW sample was driven by its lower crystallinity degree than TiO_2/GLP one, in spite of its slightly larger specific surface area (138 m^2/g). In the case of TiO_2/GLP, the improved photo-catalyst performances are mainly ascribed both to the higher crystallinity degree and to the presence the broader variety of "long-live" free-radical species photo-generated within the delocalized GLP π-electron systems, as indicated by EPR analyses. Moreover the lower free-radical density, evidenced in TiO_2/GLP, can account for the decrease of the occurrence of oxidation mechanisms of HO radical type that, producing hydroxylated undesired by-products, inevitably would lower the selectivity of the system and yields to desired products (3-PCA and NA).

4. Conclusion

Water stable GL layers, produced through a two-step oxidation/reduction wet treatment of carbon black, have been used in two different forms (in water suspension and assembled in flat blocks) to prepare composites with TiO_2 nanoparticles by liquid phase deposition (TiO_2/GLW and TiO_2/GLP, respectively). The adopted experimental approach allowed to explore the effect of morphology on catalyst performances toward selective conversion of 3-pyridine methanol to 3-pyridine carboxyaldehyde and nicotinic acid (vitamin B3), under de-aerated and UV/solar simulated conditions, in presence of cupric ions. An enhanced photocatalytic activity of TiO_2/GLP, with respect to the neat TiO_2, has been observed and attributed both to the broader variety of free-radical species stabilized within the delocalized π-electron systems of the TiO_2/GLP, as indicated by EPR analyses and to a reduction of the hydroxyl radicals formation. In the case of TiO_2/GLW, the presence of well dispersed GL layers during TiO_2 nucleation seems to interfere with the TiO_2 crystallization process lowering the composite photocatalytic activity, in spite of its higher surface area. Moreover, beneficial effects driven by the presence of highly p-conjugated systems are not observed due to the spatially confined free-radical species in TiO_2/GLW.

References

[1] C. Walling, R.W.R. Humphreys, J. Org. Chem. 46 (1981) 1260–1263.
[2] C. Parmeggiani, F. Cardona, Green Chem. 14 (2012) 547–564.
[3] M. Addamo, V. Augugliaro, M. Bellardita, A. Di Paola, V. Loddo, G. Palmisano, L. Palmisano, S. Yurdakal, Catal. Lett. 126 (2008) 58–62.
[4] V. Augugliaro, T. Caronna, V. Loddo, G. Marcì, G. Palmisano, L. Palmisano, S. Yurdakal, Chem. Eur. J. 14 (2008) 4640–4646.
[5] S. Yurdakal, G. Palmisano, V. Loddo, V. Augugliaro, L. Palmisano, J. Am. Chem. Soc. 130 (2008) 1568–1569.
[6] G. Palmisano, E. Garcıa-Lopez, G. Marcì, V. Loddo, S. Yurdakal, V. Augugliaro, L. Palmisano, Chem. Commun. 46 (2010) 7074–7089.
[7] S. Yurdakal, V. Loddo, G. Palmisano, V. Augugliaro, H. Berber, L. Palmisano, Ind. Eng. Chem. Res. 49 (2010) 6699–6708.
[8] R. Marotta, I. Di Somma, D. Spasiano, R. Andreozzi, V. Caprio, Chem. Eng. J. 172 (2011) 243–249.
[9] R. Marotta, I. Di Somma, D. Spasiano, R. Andreozzi, V. Caprio, J. Chem. Technol. Biotechnol. 88 (2013) 864–872.
[10] D. Spasiano, L.P.P. Rodriguez, J.C. Olleros, S. Malato, R. Marotta, R. Andreozzi, Appl. Catal. B: Environ. 136–137 (2013) 56–63.
[11] W.T. Chen, V. Jovic, D. Sun-Waterhouse, H. Idriss, G.I.N. Waterhouse, Int. J. Hydrogen Energy 38 (2013) 15036–15048.
[12] K. Maeda, J. Photochem. Photobiol. C: Photochem. Rev. 12 (2011) 237–268.
[13] Q. Wang, N. An, Y. Bai, H. Hang, J. Li, X. Lu, Y. Liu, F. Wang, Z. Li, Z. Lei, Int. J. Hydrogen Energy 38 (2013) 10739–10745.
[14] X. An, J.C. Yu, RSC Adv. 1 (2011) 1426–1434.
[15] S. Bai, X. Shen, RSC Adv. 2 (2012) 64–98.
[16] G. Jiang, Z. Lin, C. Chen, L. Zhu, Q. Chang, N. Wang, W. Wei, H. Tang, Carbon 49 (2011) 2693–2701.
[17] K. Zhou, Y. Zhu, X. Yang, X. Jiang, C. Li, New J. Chem. 35 (2011) 353–359.
[18] D. Wang, D. Choi, J. Li, Z. Yang, Z. Nie, R. Kou, ACS Nano 3 (2009) 907–914.
[19] Y. Liang, H. Wang, H.S. Casalongue, Z. Chen, H. Dai, Nano Res. 3 (2010) 701–705.
[20] J. Liu, H. Bai, Y. Wang, Z. Liu, X. Zhang, D.D. Sun, Adv. Funct. Mater. 20 (2010) 4175–4181.
[21] S. Stankovich, R.D. Piner, X. Chen, N. Wu, S.T. Nguyen, R.S. Ruoff, J. Mater. Chem. 16 (2006) 155–158.
[22] S. Stankovich, D.A. Dikin, R.D. Piner, K.A. Kohlhaas, A. Kleinhammens, Y. Jia, Y. Wu, S.T. Nguyen, R.S. Ruoff, Carbon 45 (2007) 1558–1565.
[23] R. Chuck, Appl. Catal. A: Gen. 280 (2005) 75–82.
[24] M. Alfè, V. Gargiulo, R. Di Capua, F. Chiarella, J.N. Rouzaud, A. Vergara, A. Ciajolo, ACS Appl. Mater. Interfaces 4 (2012) 4491–4498.
[25] S. Visentin, N. Barbero, S. Musso, V. Mussi, C. Biale, R. Ploeger, G. Viscardi, Chem. Commun. 46 (2010) 1443–1445.
[26] M.F. Ottaviani, J. Phys. Chem. 91 (1987) 779–784.
[27] N.D. Yordanov, K. Ranguelova, Spectrochim. Acta Part A 56 (2000) 373–378.
[28] R. Andreozzi, V. Caprio, A. Insola, R. Marotta, Water Res. 34 (2000) 463-472.
[29] L. Panzella, G. Gentile, G. D'Errico, N.F. Della Vecchia, M.E. Errico, A. Napolitano, C. Carfagna, M. d'Ischia, Angew. Chem. Int. Ed. 52 (2013) 12684–12687.
[30] A. Pezzella, L. Capelli, A. Costantini, G. Luciani, F. Tescione, B. Silvestri, G. Vitiello, F. Branda, Mater. Sci. Eng. C 33 (2013) 347–355.
[31] E. Cesareo, L. Korkina, G. D'Errico, G. Vitiello, M.S. Aguzzi, F. Passarelli, J.Z. Pedersen, A. Facchiano, Plos One 7 (2012) e48849.
[32] F. Zuo, L. Wang, T. Wu, Z. Zhang, D. Borchardt, P. Feng, J. Am. Chem. Soc. 132 (2010) 11856–11867.
[33] E.A. Konstantinova, A.I. Kokorin, S. Sakthivel, H. Kisch, K. Lips, Chim. Int. J. Chem. 61 (2007) 810–814.
[34] M. Long, Y. Qin, C. Chen, X. Guo, B. Tan, J. Phys. Chem. C 117 (2013) 16734–16741.
[35] I. Nakamura, N. Negishi, S. Kutsuna, T. Ihara, S. Sugihara, K. Takeuchi, J. Mol. Catal. A: Chem. 161 (2000) 205–212.
[36] L. Ćirić, A. Sienkiewicz, R. Gaál, J. Jaćimović, C. Vâju, A. Magrez, L. Forrò, Phys. Rev. B 86 (2012) 195139.
[37] E.B. Li, X.Z. Li, M.F. Hou, K.W. Cheah, W.C.H. Choy, Appl. Catal. A 285 (2005) 181–189.
[38] J. Yu, J.C. Yu, M.K.P. Leung, W. Ho, B. Cheng, X. Zhao, J. Zhao, J. Catal. 217 (2003) 69–78.
[39] J. Ovenstone, J. Mater. Sci. 36 (2001) 1325–1329.